Journal of Magnetism and Magnetic Materials 497 (2020) 165968

Contents lists available at ScienceDirect

Journal of Magnetism and Magnetic Materials

journal homepage: www.elsevier.com/locate/jmmm

Research articles

Nd ordering, cluster formation, and the origin of negative magnetization in $NdMn_{0.8}Fe_{0.2}O_{3+\delta}$

D.M. Pajerowski[a,*], C.A. Escanhoela Jr.[b,c], D. Haskel[b], T.R. Prisk[d], M.D. Frontzek[a], D. Phelan[e], M. Mihalik Jr.[f], M. Mihalik[f]

[a] Neutron Scattering Division, Oak Ridge National Laboratory, Oak Ridge, TN 37831, USA
[b] Advanced Photon Source, Argonne National Laboratory, Argonne, IL 60439, USA
[c] Brazilian Synchrotron Light Laboratory, Brazilian Center for Research in Energy and Materials, Campinas, SP 13083-970, Brazil
[d] Center for Neutron Research, National Institute of Standards and Technology, Gaithersburg, MD 20899, USA
[e] Materials Science Division, Argonne National Laboratory, Argonne, IL 60439, USA
[f] Institute of Experimental Physics, SAS, Watsonova 47, Kosice, Slovakia

ABSTRACT

The orthorhombic pseudo-perovskite series $NdMn_{1-x}Fe_xO_{3+\delta}$ has negative magnetization, i.e. magnetization directed opposite to an applied field under certain conditions, for x = 0.2 and x = 0.25. We have investigated the microscopic origin of this phenomenon for x = 0.2 by using elastic and inelastic scattering techniques including neutron backscattering, X-ray magnetic circular dichroism at the Mn *K* and Nd L_2 edges, neutron powder diffraction, and powder inelastic neutron scattering. We find that Nd^{3+} ions possess zero field ordered moments of 1.6 μ_B per ion at 1.5 K oriented parallel to the Mn moments. Based upon the neutron diffraction, there is a freezing of magnetic clusters before the long-range order sets in. The Nd crystal field levels shift with temperature due to a molecular field that is 1.1 meV at 1.5 K. These findings are consistent with a magnetic domain/cluster model for the negative magnetization in $NdMn_{0.8}Fe_{0.2}O_{3+\delta}$.

1. Introduction

Manganites that can display colossal magnetoresistance (CMR) have been studied extensively in the $R_{1-x}A_xMnO_3$ hole doped series, where R is a rare earth metal and *A* is an alkali metal [1]. Of these, the $La_{1-x}Ca_xMnO_3$ has been most highly investigated for its complex interplay between magnetic, charge, and structural order that affect the CMR [2]. Among further explorations, it was found that changing the A-site ions can modulate the bandwidth and exchange interactions, and changes to the CMR are seen in the $Nd_{1-x}Ca_xMnO_3$ series [3]. A yet additional dimension of study is afforded by B-site doping, and the iron doped manganite series has been studied to understand its magnetic properties [4–9] and more recently for the understanding of possible multiferroism [10]. This paper presents experiments on the x = 0.2 compound of the $NdMn_{1-x}Fe_xO_{3+\delta}$ (NMFO) series ($NdMn_{0.8}Fe_{0.2}O_{3.065}$ = **NMFO.2**) and focuses on its intriguing magnetic response.

The magnetic response of **NMFO.2** has been reported to have a complicated behavior [5]. There is an initial up-turn of the magnetization upon cooling indicative of ferromagnetism, followed by an additional inflection and a down turn with zero-crossing and sign reversal indicating magnetization that opposes the applied field, Fig. 1. This observed magnetization compensation and subsequent magnetic pole reversal is unique to dopings in the vicinity of **NMFO.2** (e.g. x = 0.2 and x = 0.25), which is in the region near the minimum ordering temperature of $NdMn_{1-x}Fe_xO_{3+\delta}$ as a function of x [4,5]. Negative magnetization, whereby the magnetization of the sample is opposite to the applied magnetic field under certain conditions, has been reported in analogous compounds and can be caused by a variety of sources that include sublattice compensation and magnetic domain compensation [11]. The presence of three magnetic ions in the system has made modelling and assignment of ionic contributions to the magnetic response difficult.

The three magnetic ions in NMFO are Nd, Mn, and Fe and have well studied single-ion magnetic properties [12]. The Nd^{3+} ion is the most complex of the lot and has a $4f^3$, 10-fold degenerate ^4I_J (S = 3/2, L = 6, J = |L − S|… |L + S|, m_J = −J … J) ground state, which is split and mixed in the distorted perovskite host lattice, and the ground state spin momentum is antiparallel to the net moment. The Mn^{3+} ion in $NdMnO_3$ (NMO), akin to **NMFO.2**, is similar to that in $LaMnO_3$ (LMO), $3d^4$ with a Jahn-Teller ^5E_g ground state (here S = 2 and m_S are good quantum numbers, and there is no first order orbital moment), although subtle differences arise from the smaller ionic radius and larger electronegativity of Nd compared to La. The Fe^{3+} ion in $NdFeO_3$ (NFO) has a half-full d-shell $^6A_1$ ground state (S = 5/2). The Mn^{4+} ion in an octahedral field is a $3d^3$, half-full t_{2g} with a $^4A_2$ ground state.

* Corresponding author.
E-mail address: pajerowskidm@ornl.gov (D.M. Pajerowski).

https://doi.org/10.1016/j.jmmm.2019.165968
Received 27 February 2019; Received in revised form 18 September 2019; Accepted 7 October 2019
Available online 09 October 2019
0304-8853/

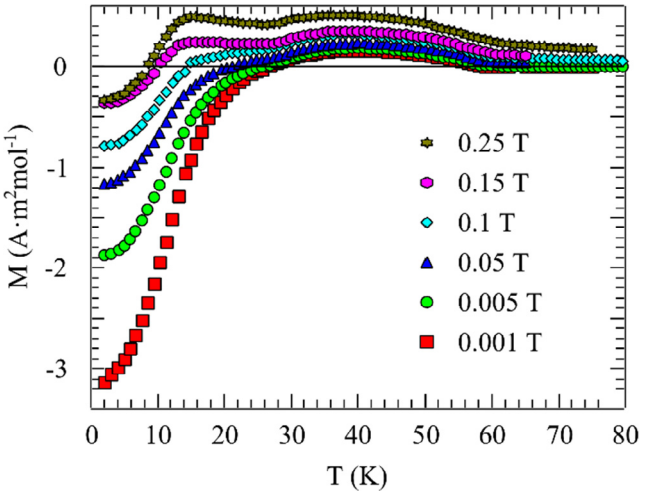

Fig. 1. Field-cooled magnetization of **NMFO.2**.

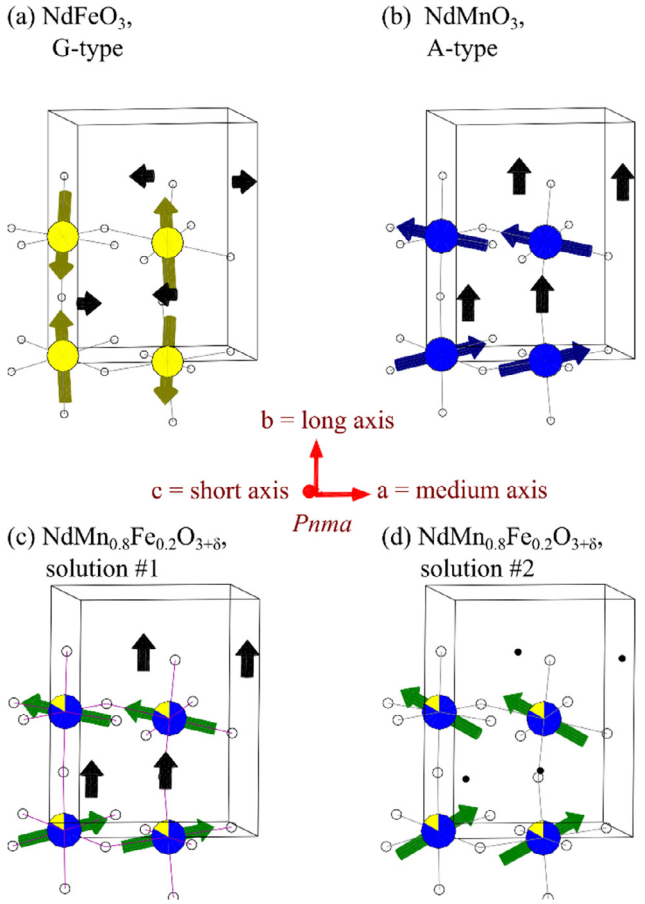

Fig. 2. Magnetic structures of end-member compounds and two neutron diffraction solutions for **NMFO.2**. Temperatures of the structures are below the magnetic order of the transition metals and induced ordered rare-earth moments, but above the ~1 Kelvin where Nd-Nd interactions play a role. (a) Iron is represented by yellow colors, (b) manganese is represented by blue, and for (c-d) $NdMn_{0.8}Fe_{0.2}O_{3+\delta}$ the arrows are an average of Mn and Fe moments. Neodymium is shown as a small dot, with black arrows for those magnetic moments. Oxygen is a small open circle. (For interpretation of the references to colour in this figure legend, the reader is referred to the web version of this article.)

These magnetic ions hosted on a pseudo-perovskite lattice give rise to long-range magnetic order of different types. For all values of x, NMFO crystallizes in the distorted perovskite orthorhombic space group isostructural to $GdFeO_3$ that may be notated as Pnma [13]. The NFO end-member compound is a G-type antiferromagnet, Fig. 2 (a), with $T_N = 690$ K [14,15] and increased Nd electronic magnetism concomitant with increased Fe weak ferromagnetism below $T_{Nd} \approx 4$ K [16,17]. In fact, NFO shows a magnetic compensation at 7.6 K that is explained with competing Nd and Fe magnetic sublattices [18]. Manganese doping of NFO destroys the magnetic compensation, as seen in a compound of $NdMn_{0.15}Fe_{0.85}O_3$ [6]. The NMO end-member compound is an A-type antiferromagnet, Fig. 2 (b), with $T_N = 82$ K and increased Nd magnetism concomitant with increased Mn weak ferromagnetism below $T_{Nd} \approx 20$ K [19]. The **NMFO.2** was recently studied with neutron diffraction, which can detect magnetic moments on unique crystallographic sites but not necessarily with elemental specificity, so neodymium local moments may be refined as can an average of the iron and manganese moments. Two magnetic structure models reproduce the neutron diffraction with similar residuals: solution #1 with neodymium polarized along the b-axis (Fig. 2 (c)), and solution #2 with no neodymium contribution (Fig. 2 (d)) [8]. Solution #1 has sublattice magnetizations of $\mu_{Mn,Fe} = (-2.96, 0.19, 0.8)\ \mu_B$ and $\mu_{Nd} = (0, 1.65, 0)\ \mu_B$ and solution #2 has sublattice magnetizations of $\mu_{Mn,Fe} = (3.16, 1.96, 0.8)\ \mu_B$ and $\mu_{Nd} = (0, 0.05, 0)\ \mu_B$, where the ordering types are $\mu_{Mn,Fe}$ = (A, F, G) and μ_{Nd} = (-, f, -) with A and G being antiferromagnetic while F and f are ferromagnetic; the only net moment is along the crystallographic b-axis. Indeed, preliminary results from this present work were included in the discussion of neutron diffraction results in reference [8]. The physics behind the two models is quite different as solution #1 would assign the second inflection to a neodymium participating ferromagnetism akin to NMO [19], while solution #2 invokes an Mn/Fe spin-reorientation akin to the NFO end-member [20].

Therefore, the stage is set to pose two questions about the magnetism in **NMFO.2**: (1) what is the nature of the second phase transition observed in neutron powder diffraction, magnetization, and specific heat? (2) what causes the negative magnetization observed in **NMFO.2**? To answer these questions, we have performed experiments with a slant towards elemental specificity (neutron backscattering spectroscopy, X-ray magnetic circular dichroism), those probing spatial correlations at different length scales (neutron powder diffraction), and those probing the energetics of neodymium interactions (inelastic neutron scattering).

Neutron backscattering spectroscopy (NBS) is an element-specific probe for measuring ordering of Nd^{3+} electronic moments by way of the hyperfine interaction with the nuclear spin levels, which falls in the range of energy transfer probed by NBS. Following the analysis used for NFO [17], the nuclear energy splittings observed by NBS are proportional to the hyperfine field, and are also proportional to the hyperfine coupling times the electronic magnetic moment. Previous work on the end member compounds NMO [21] and NFO [17] demonstrated that there is a nearly linear dependence of the coherent Nd moment with the observed hyperfine splitting for samples containing naturally abundant isotope ratios of Nd.

A second element-specific probe of the magnetic ordering is X-ray magnetic circular dichroism (XMCD) with hard X-rays, which can be applied on both the Nd *L* edges and the Mn *K* edge. Indeed, this technique has previously been applied to investigate the microscopic origin of the negative magnetization effect in oxygen-rich $NdMnO_{3.11}$ [22]. By tracking Mn and Nd magnetizations as a function of temperature and applied field, a domain effect due to phase separation was ascribed as the source of the negative magnetization. This explanation was consistent with the observation of negative magnetization in Ca doped NMO as a result of phase separation [23]. In the model for doped NMO, when Mn^{4+} ions are present in appreciable quantity, Mn^{4+}-Mn^{3+} ferromagnetic clusters stabilized by double exchange interactions then interact with (weakly-ferromagnetic) antiferromagnetic regions to give

rise to negative magnetization in low-applied-magnetic fields.

In addition to the element specific probes described above, we have also employed conventional neutron powder diffraction (NPD). In contrast to previous work by some of the authors [8], we have focused on the low momentum-transfer (Q) region that is sensitive to short-range (magnetic) order. The higher Q scattering has already been employed to investigate the magnetic ground state of NMO [19], NFO [16,20], and specifically the **NMFO.2** sample of direct interest here [8]. In $NdMnO_{3.11}$, a qualitative analysis of the data below $Q \approx 0.4\,\text{Å}^{-1}$ showed an additional order parameter in the system that was associated with ferromagnetic clusters forming in regions rich in Mn^{4+}-ions [22]. In addition, we have performed neutron diffraction on instruments that have energy analysis and can separate fluctuating versus static contributions to clustering.

Finally, we have employed powder inelastic neutron scattering (PINS) to investigate the magnetic excitations of **NMFO.2**, focusing on the neodymium excitations. PINS is expected to contain contributions due to spin waves, crystal field excitations, and phonons [24]. For these powder data, we focus on the crystal field excitations. Neodymium crystal field excitations have been measured by PINS in $NdGaO_3$ [25] and NFO [26], and the similar peak positions and amplitudes in both systems suggest that the electronic structure of Nd is similar, albeit not identical, in those systems.

Following this introduction, Section II has the experimental results of the four techniques that were introduced and discusses the implications of the observations to Nd ordering, cluster formation, and the origin of negative magnetization. A qualitative picture of the magnetization consistent with the experimental observations is generated. Section III has summarized conclusions. Technical details are reported in Appendix A.

2. Results and discussion

2.1. Magnitude of neodymium coherent moment

From the hyperfine excitations measured in NBS, the magnitude of the coherent neodymium moment was extracted as a function of temperature to confirm if Fig. 2 (c) or (d) is more appropriate to model **NMFO.2**. Energy scans show the evolution of an inelastic signal upon cooling, and four examples of data with fits are shown in Fig. 3 (a) and (b). The fitting function has three parameters that change with temperature: a constant background, the intensity of the elastic peak, and the energy shift of the Nd^{3+} mode. This hyperfine energy shift is used to extract the coherent Nd electronic magnetic moment, and the splitting is nonzero from T_N and has an upturn when cooling below T_{Nd}, Fig. 3 (c). At the lowest temperature measured, the neodymium moment is found to saturate to 1.63 ± 0.01 μ_B. This magnetic moment is extracted from the energy splitting, ΔE_{Nd}, of 2.07 ± 0.01 μeV and the relation 0.79 μ_B/μeV that was found by considering NBS of various neodymium containing compounds [21]. For NMO at T = 2 K, different spectrometers yielded ΔE_{Nd}, of 2.06 ± 0.02 μeV and ΔE_{Nd}, of 2.15 ± 0.02 μeV [21]. For NFO at T = 2 K, ΔE_{Nd} = 1.02 μeV [17]. So, the **NMFO.2** looks to have identical behavior of the moment magnitude to the NMO but different than the NFO, and only one resolution-limited peak was observed. The temperature dependence of the background, as well as a confirmation of the elastic magnetic order parameters are given in the Supplemental Material [27].

2.2. Neodymium molecular field

Confirmation of the neodymium single-ion wavefunctions and measurement of the neodymium molecular field is obtained from the crystal field transitions measured by triple-axis PINS. Four crystal field excitations were observed above T_N for **NMFO.2** at 9.4 meV, 22.8 meV, 47.8 meV, and 61.5 meV, with intensities relative to the strongest peak of 1.00, 0.30, 0.50, and 0.26, respectively. The ≈9 meV separation of

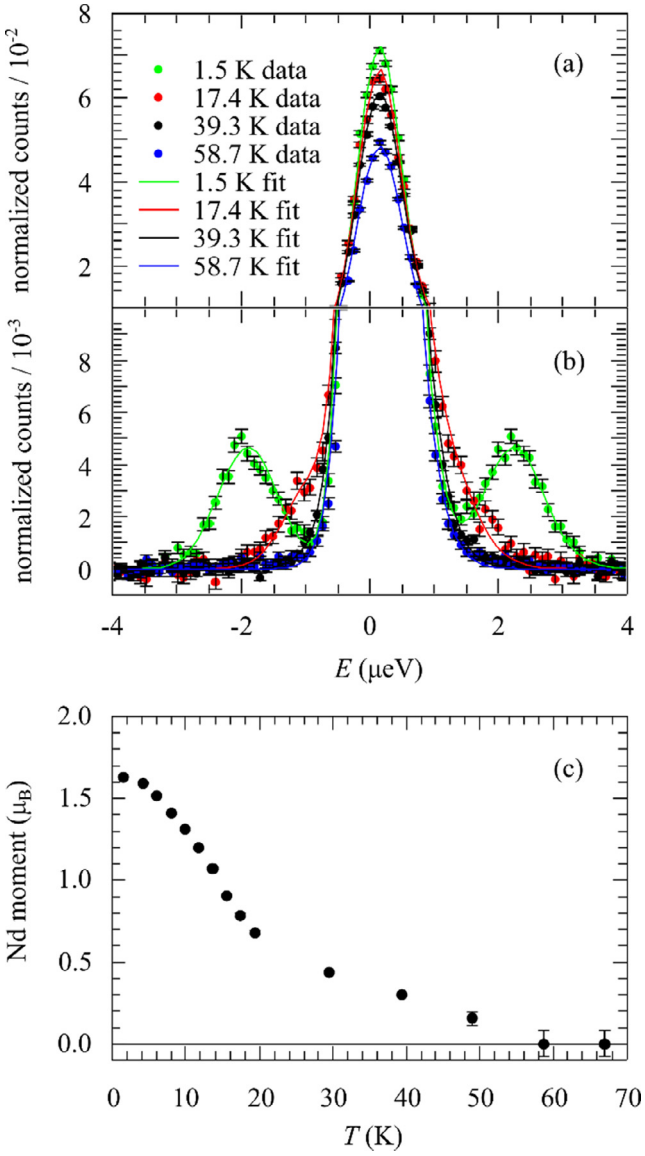

Fig. 3. Neutron backscattering spectroscopy of **NMFO.2.** Integrating from $Q \approx 0.25\,\text{Å}^{-1}$ to $1.75\,\text{Å}^{-1}$, the intensity of (a) the elastic signal and (b) the inelastic scattering are shown. Uncertainty bars are from counting statistics and represent one standard deviation. (c) The inelastic energy transfer converted to electronic magnetic moment. Uncertainty bars are from least-squares fitting.

the ground state to the first excited state corresponds to an equivalent temperature of 104 K, so at temperatures below 50 K the ground state Kramers doublet is 90% populated and by 20 K the ground state Kramers doublet is > 99% populated and only two Nd states are relevant to the magnetic properties. The two largest contributions to the ground-state doublet wavefunction of NMO are 0.699|J = 9/2, $m_J = \pm 5/2$ > and 0.486|J = 9/2, $m_J = \pm 9/2$ > [28].

To investigate molecular field effects, the crystal field excitations were measured at temperatures below the onset of magnetic order. This molecular field provides information about the interactions between Nd^{3+} and other ions in the lattice, which may be magnetostatic or arise from superexchange. For these measurements, the momentum transfer was chosen such that spin wave contributions were minimal while phonons remained significant, Fig. 4 (a). The neodymium specific contribution in **NMFO.2** can then be estimated by subtracting the (Savitzky-Golay smoothed) [29] **LMFO.2** phonon signal to reveal two clear peaks in this energy range that shift with temperature, Fig. 4 (b). A detailed temperature dependence of shifts in the crystal field levels is

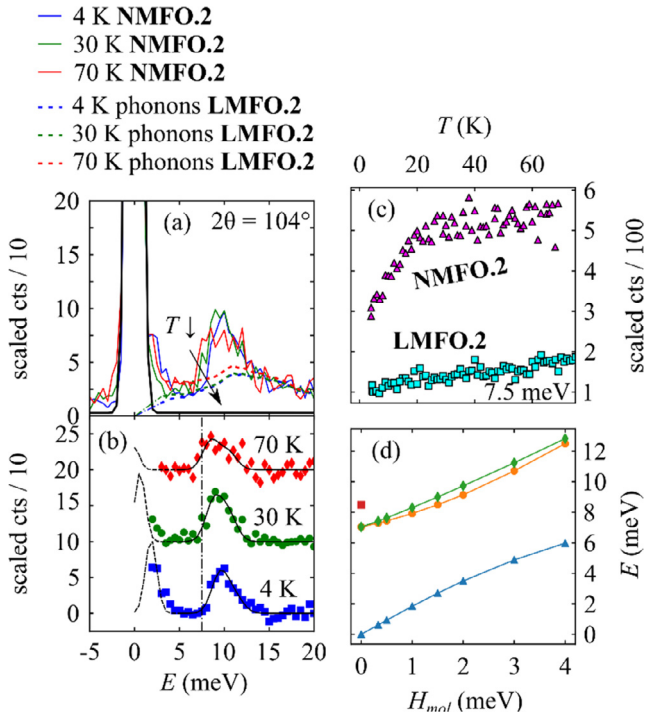

Fig. 4. Temperature dependent powder inelastic neutron scattering measured on thermal triple-axis. (a) Energy scans showing the magnetic excitations. (b) Crystal field excitations after subtraction **LMFO.2** from **NMFO.2**. These data have been offset for clarity. (c) Temperature dependence of intensity at 7.5 meV and 2θ = 104°. (d) The first three Nd crystal field levels increase as a function of molecular field calculated using the Wybourne parameters fit by infrared [28] with the infrared measured value with no molecular field as a single red square. (For interpretation of the references to colour in this figure legend, the reader is referred to the web version of this article.)

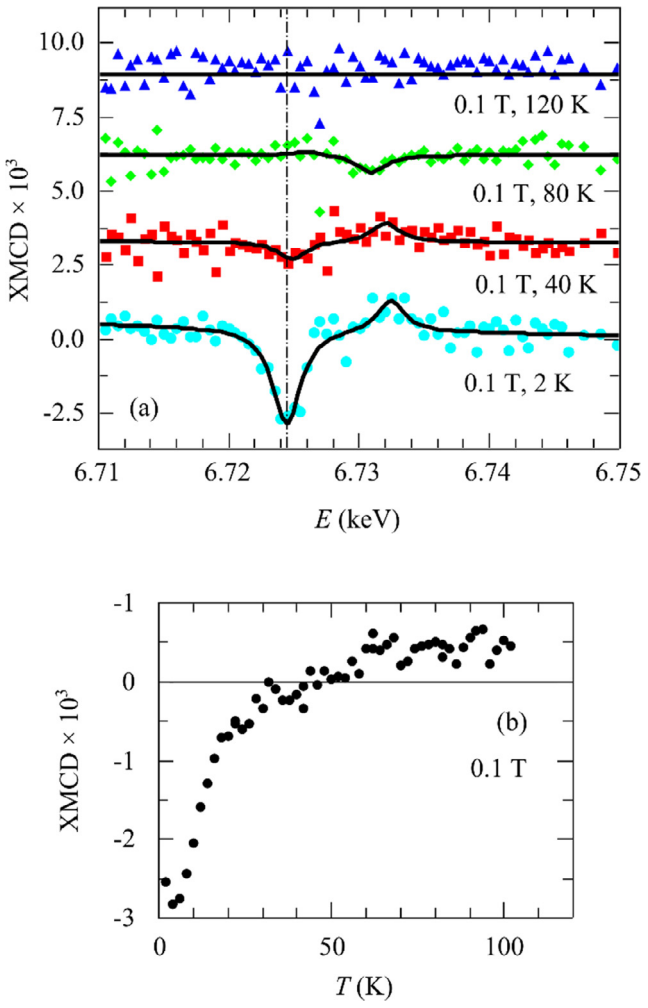

Fig. 5. Temperature dependence of X-ray magnetic circular dichroism at the Nd L_2 edge of **NMFO.2**. (a) The XMCD energy scans show the magnetic reversal in the lobes, where black lines are fits with Lorentzian peaks. These data have been offset for clarity. (b) Temperature dependence of the intensity at the larger lobe is plotted.

measured by aligning the spectrometer to take data near the edge of one transition, and an inflection of that intensity is observed near 15 K, Fig. 4 (c). The 70 K data can be fit by two resolution-limited Gaussians with energies of the pure end members, 8.48 meV (as for NMO) [28] and 10.4 meV (as for NFO) [26], suggesting some degree of Mn and Fe phase separation. By 30 K, the lower energy Gaussian has shifted to 8.8 meV, while the higher energy Gaussian remains at 10.4 meV. At 4 K, the lower energy peak has further shifted to 9.5 meV and the higher energy peak has shifted to 11.1 meV. For the case of Mn-rich regions, to which the lower energy peak near 9 meV is ascribed, the reported NMO single-ion parameters are used to calculate the transition energy as a function of molecular field along the ferromagnetic crystallographic b axis [28]. Those NMO parameters were done globally over many infrared absorptions as a function of magnetic field and small errors are present for individual levels, such that our observations of the third and fourth states (the first excited Kramer's doublet) differ from those in the parameter set. Therefore, we use energy shifts from the parameter set, rather than absolute positions. These shifts of the lowest energy levels are shown in Fig. 4 (d), and result in H_{mol} = 0.3 meV at 30 K and H_{mol} = 1.0 meV at 4 K. The observed energies are not magnetostatic, which has an energy scale of less than ≈1 K for the Nd in this system. Those extracted molecular fields then reproduce the intensity and position of the splitting of the ground state doublet that is ≈2 meV at 4 K, which corresponds to an equivalent temperature of 23 K such that > 99% of the ground-state doublet will be in the exchange lowered magnetic singlet at 4 K. The molecular field induced Nd^{3+} magnetic moments in this crystal-field Hamiltonian model may then be calculated to give m_{Nd}[4 K] = (0, 1.50 μ_B, 0) and m_{Nd}[30 K] = (0, 0.25 μ_B, 0), which are similar to the moments measured with NBS. A comparison of spin-wave to crystal field intensities, lower momentum data, plots of higher energy crystal fields, and Q-E trajectories of the scans are available in the Supplemental Material [27].

2.3. Temperature dependence of neodymium moment direction in low field

Having confirmed that Nd has long-range magnetic order, we consider the sign of the Nd magnetization to help understand the negative magnetization in Fig. 1. The temperature dependence of the direction of the neodymium magnetization in **NMFO.2** can be extracted from the Nd L_2 edge XMCD, as was done in $NdMnO_{3+\delta}$ [22]. Similar to the neodymium response in $NdMnO_{3+\delta}$, there are two main features: a large lobe that is positive when the magnetization is along the applied field, and a smaller side lobe at higher energy and of an opposite sign. This Nd-specific XMCD signal for fields of 0.1 T is negligible at 120 K, shows small magnetization along the applied field direction at 80 K, grows stronger and has inverted by 40 K, and is greatly increased and still opposed to the applied field at 2 K, Fig. 5 (a). Sitting at the energy of the strongest XMCD lobe after field cooling in 0.1 T, a finely stepped temperature dependence, Fig. 5 (b), more precisely shows the evolution of the magnetization reversal, although the zero offset includes a background contribution. The order parameter as a function of temperature has an inflection point near 20 K and one near 60 K. Ultimately, these data show that the Nd moment is opposite to the 0.1 T

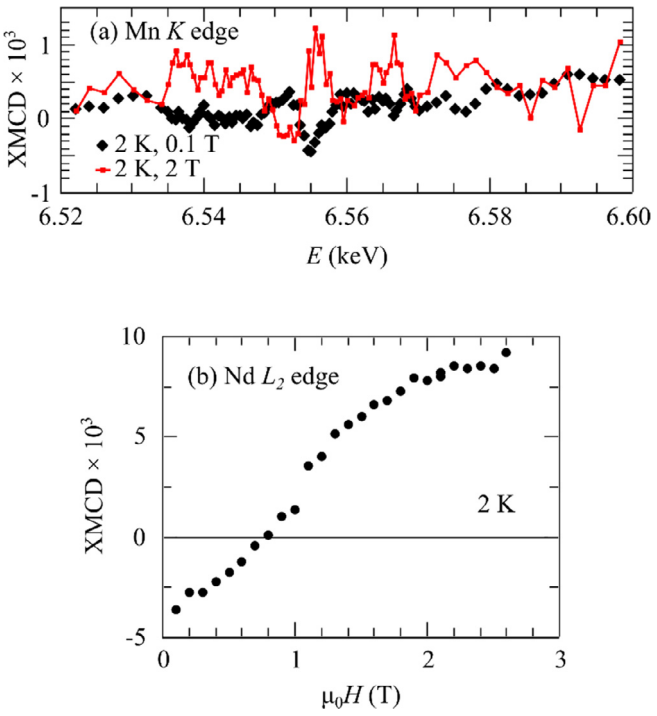

Fig. 6. Magnetic field dependence of X-ray magnetic circular dichroism of **NMFO.2**. (a) The Mn *K* edge energy scans and (b) the intensity of the larger lobe on the Nd L_2 edge are shown.

applied field when **NMFO.2** is magnetically ordered. The unpolarized neodymium XAS edge is available in the Supplemental Materials [27].

2.4. Magnetic field dependence of neodymium and manganese magnetization orientations at low temperature

If the macroscopic magnetizations of Nd and Mn are oppositely aligned, then different temperature dependences of the ordered moments could give rise to negative magnetization. To test this possibility, the relative orientations of manganese and neodymium are obtained from XMCD. Like the Nd L_2 edge, the Mn *K* edge has a dichroic signal that is correlated to the electronic magnetic moment. The Mn K edge response is found to be similar to that seen in $NdMnO_{3+\delta}$ [22], grossly consisting of a 'w' shape with the central peak near 6.555 keV for magnetization parallel to the applied field that inverts to an 'm' shape for magnetization antiparallel to the applied field. At 2 K, after field cooling in 0.1 T, the manganese magnetization is antiparallel to the applied field, and at some field less than 2 T the manganese moment is coerced to be parallel to the applied field, Fig. 6 (a). The unpolarized manganese XAS edge is available in the Supplemental Materials [27]. For neodymium, in the same 0.1 T field cooled configuration as the aforementioned temperature dependence, the order parameter of the strongest lobe as a function of magnetic field has a sign change near 0.75 T at 2 K, Fig. 6 (b). For the conditions measured, the neodymium and manganese macroscopic magnetizations are parallel. This locking of Mn and Nd orientations for the experimental temperature and field regions probed is consistent with the large molecular field acting on Nd measured with PINS. By way of comparison, the single-ion Hamiltonian for Nd^{3+} used in to model PINS with the 1 meV molecular field at 4 K would require an oppositely applied magnetic field of 15 T to reorient the Nd moments, which suggests that the energy scale for the field-induced sign change in magnetization of **NMFO.2** is not set by Nd-Mn interactions. Importantly, the observation that Nd and Mn have the same sign impedes a sublattice reversal model. Moreover, the similarity between the XMCD of **NMFO.2** and the $NdMnO_{3+\delta}$ shows that the root cause of the effect is related, and the $NdMnO_{3+\delta}$ authors invoked a

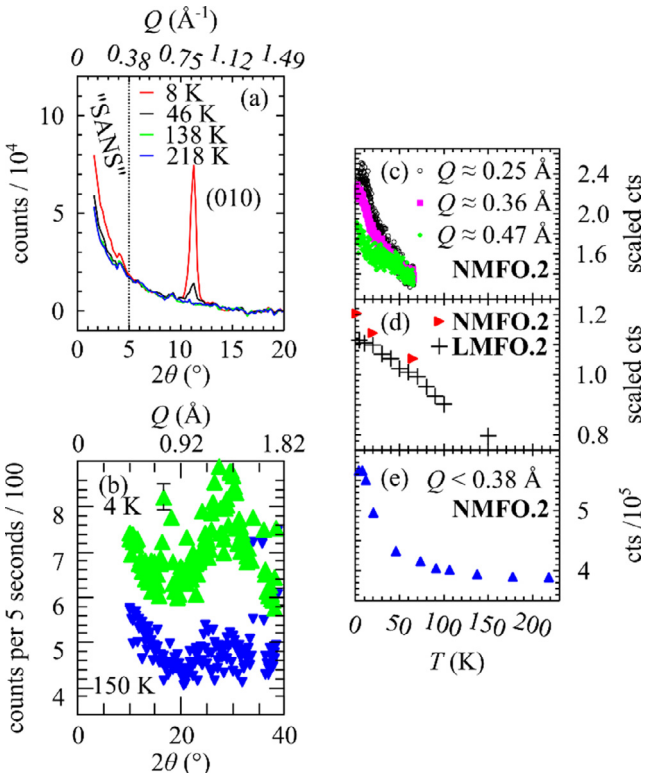

Fig. 7. Elastic neutron scattering. (a) Powder diffraction of **NMFO.2** without energy analysis showing the presence of a magnetic Bragg peak and the "SANS" region. (b) Powder diffraction of **LMFO.2** with energy analysis on a triple-axis spectrometer, with one statistical uncertainty bar shown. (c) Powder diffraction of **NMFO.2** on a backscattering spectrometer. (d) Low angle diffuse scattering with energy analysis on a triple-axis spectrometer. (e) The "SANS" signal from a powder diffractometer without energy analysis.

domain model for that system, which was further supported by observation of a temperature dependent small angle signal in the diffraction [30]. In the next subsection, we present small angle diffraction of **NMFO.2**.

2.5. Magnetic clusters

Having ruled out a sublattice model of negative magnetization, another mechanism must be responsible. Magnetic clusters observed with neutron diffraction explained the negative magnetization in $NdMnO_{3+\delta}$, so **NMFO.2** and **LMFO.2** were measured to compare the short-range magnetic correlations between the three compounds. Short-range magnetic order manifests in NPD as diffuse signals concentrated in the small angle neutron scattering (SANS), but possibly at higher angles depending upon the length scale.

In addition to the known temperature dependence of the long-range magnetic ordering in **NMFO.2**, a temperature dependent signal was observed using a powder diffractometer for momenta less than $Q = 0.38\,Å^{-1}$, Fig. 7 (a). Such diffractometers do not have energy analysis, and a thermal diffuse component (that includes paramagnetic contributions) was subtracted from the diffractometer data in Fig. 7. These $Q < 0.38\,Å^{-1}$ scattering events arise from d-spacings > 16 Å. A detailed temperature dependence of the **NMFO.2** diffractometer "SANS" shows gradual increase below 200 K with a subtle inflection near T_N and a more pronounced inflection near T_{Nd}, Fig. 7 (e).

A triple-axis spectrometer with energy discrimination (≈1.4 meV resolution) showed diffuse elastic scattering at low angles for **LMFO.2** that similarly increased when lowering the temperature, Fig. 7 (b). Conversely, for a strictly paramagnetic to magnetically ordered transition, the elastic background is larger at higher temperatures due to

paramagnetic scattering that transfers intensity into magnetic Bragg peaks for the ordered state. These spectrometer data show increased low-temperature non-ordered scattering at even smaller d-spacings, albeit with lesser intensity. The temperature dependence of the triple-axis diffuse scattering data for **LMFO.2** and **NMFO.2** is similar, although **NMFO.2** has an inflection at T_{Nd}, Fig. 7 (d). The correlations of the small angle scattering intensity changes with the long-range-magnetic-order shows a connection between the two features and suggests assignment of the small angle signal to magnetic clusters. In such a picture, both **NMFO.2** and **LMFO.2** have magnetic clusters with strong cluster signatures below T_N, but persisting above T_N, and in **NMFO.2** the small angle scattering signal increase below T_{Nd} is consistent with ferromagnetic clusters that increase when Nd long-range order sets in.

The NBS with the highest energy precision ($\approx$0.7 μeV resolution) also shows scattering in **NMFO.2** that becomes more intense at lower momenta and at lower temperatures, Fig. 7 (c). This energy resolution sets the timescale for such clusters to be nanoseconds or slower. Moreover, the observation of the non-ordered signal in different instruments shows this feature is not an experimental artifact. So, iron doping may give rise to magnetic clusters that are strongly correlated above the ordering temperature for **LMFO.2** and **NMFO.2** analogous to how Mn^{4+} doping evolves magnetic clusters above T_N in $NdMnO_{3+\delta}$. A key difference is that Mn^{4+} are mobile in the manganite lattice, while Fe^{3+} moieties are immobile at the temperatures probed here. The temperature dependence of the thermal diffuse scattering from the powder diffractometer, as well as the elastic magnetic order parameters of **NMFO.2** and **LMFO.2**, are available in the Supplemental Materials [27].

2.6. Qualitative model

The emerging picture of the magnetic response of **NMFO.2** as a function of field and temperature may be illustrated with a cartoon, Fig. 8. At a high enough temperature, the **NMFO.2** is paramagnetic. At a temperature less than the Néel temperature of NFO, $T_{CLUSTER}$, Fe-rich regions will undergo a type of magnetic freezing to give rise to magnetic clusters that are not spatially coherent on diffraction length scales (no Bragg peaks) but have long time coherence. The notion that the iron spins are already frozen in at T_N is consistent with the entropy measured for $NdMn_{1-x}Fe_xO_3$, where only the entropy associated with the Mn spins is accounted for across the magnetic long-range order phase transition [5]. For any doped system, there will be clustering associated with the chemical order (here Mn and Fe on the crystallographic B-site), even if atoms are statistically distributed. Although there is a complicated fractal nature of such clustering, a mean cluster size (s_{mean}) can be approximated when assuming a random chemical distribution in the dilute limit [31]. This approximation of the minority atoms in $NdMn_{1-x}Fe_xO_{3+\delta}$ gives $s_{mean}(x = 0.1) = 1.1$ Fe atoms, $s_{mean}(x = 0.2) = 5.66$ Fe atoms, and $s_{mean}(x = 0.25) =$ Fe 16.0 atoms. These Fe-rich clusters will affect the domain structure of the weak ferromagnetism within the long-range ordered Mn-rich regions that develops below T_N. These magnetically dilute, Fe-rich clusters will have time-averaged magnetizations that are along a perturbatively small applied field. When Mn-rich regions that support long-range magnetic order begin to have strong correlations at T_N, the Fe-rich clusters along the field will cause a bias in the domain populations such that the predominance of Mn-rich regions are against the lab field even while the net magnetic response of all regions together is along the applied field. The antiparallel alignment of weak ferromagnetism in Mn versus weak ferromagnetism in Fe may be magnetostatic, or due to the antiferromagnetic superexchange between Mn and Fe in orthoferrites [32]. Indeed, the 1 Tesla energy scale of the isothermal magnetization reversal is near the coupling energy of weak ferromagnetism between Mn and Fe in NMFO ($\approx 0.1\ \mu_B$ canted ferromagnetic moment components coupled via $\approx$2 meV superexchange). The negative magnetization may then occur when neodymium polarization sets in for Mn-rich regions, which only increases

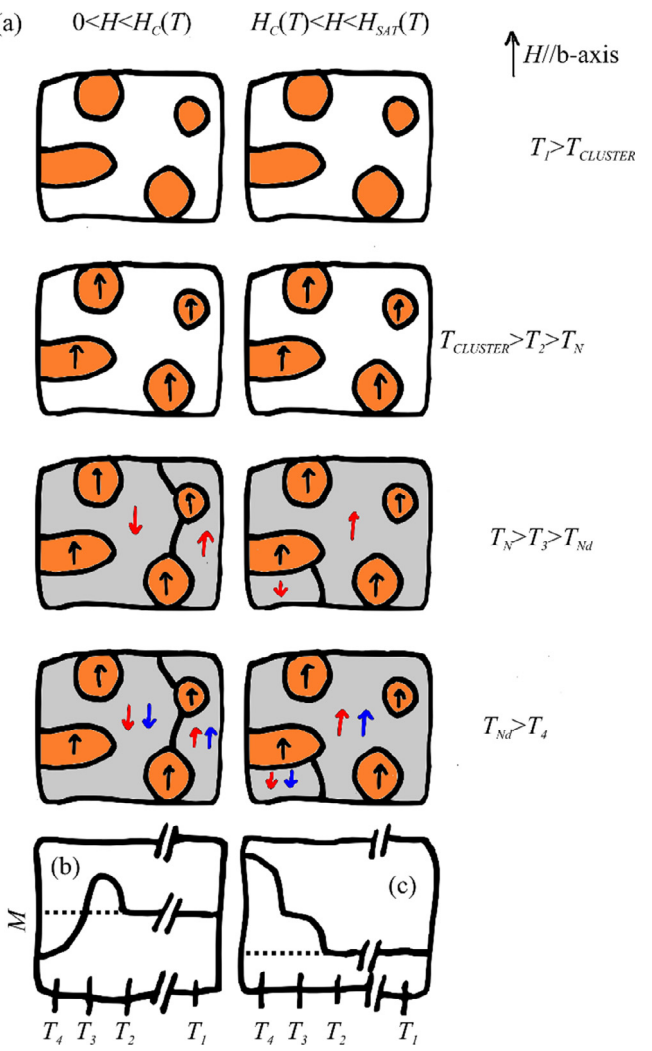

Fig. 8. Cartoon schematic of magnetization in **NMFO.2**. (a) Two different field regimes visualizing the spatial extent of magnetization are shown at different temperatures on the nanoscale. Orange regions are Fe-rich, white regions are Mn-rich in the paramagnetic state, and gray regions are Mn-rich in the long-range ordered state. Black arrows represent Fe-rich magnetization direction, red arrows represent Mn-rich magnetization direction, and blue arrows represent the additional Nd magnetism. An illustration of the bulk magnetization for (a) the low-field regime and (b) the high-field regime defines the visualized temperatures, where the zero magnetization line is shown as a horizontal dotted line. (For interpretation of the references to colour in this figure legend, the reader is referred to the web version of this article.)

the response of the domains that had been set against the applied field. So, for sufficiently low magnetic fields, the domain structure can give rise to a negative magnetization below T_{Nd}, as the domain structure is locked into a metastable magnetostatic state at the higher temperatures. For sufficiently high magnetic fields above some temperature dependent critical field, H_C, the Zeeman effect overcomes the cluster interactions and negative magnetization is destroyed.

There is a narrow Fe-doping window at which clusters are expected to be present at a sufficient population to affect the domains without changing the magnetic structure. Above a critical doping, the cluster picture is no longer applicable. For example, the percolation limit of a simple cubic lattice is x = 0.3116077 [33]. However, NMFO samples are more complicate than a simple percolation, and at an x value lower than 0.31 the G-type iron phase dominates the long range order of the lattice.

The line of thinking may be compared to similar compounds. For example, negative magnetization would not be expected in an

analogous system with a non-magnetic A-site, as in lanthanum based systems, as the recipe proposed requires some energy that will change the domain magnetization after the domain structure is set. Consistently, the **LMFO.2** sample did not show any negative magnetization. Similarly, for the lanthanum based orthomanganite in which there may even be Mn^{4+} ions present as in $NdMnO_{3.11}$, no negative magnetization was observed for $LaMn_{1-x}Fe_xO_3$ ($0 < x < 0.4$) [9]. On the other hand, there are many reported cases of negative magnetization for perovskites, of which some are explained as competition between competing sublattices and others by magnetic domain pinning [11]. After reference [11] was published, a magnetization reversal was observed in single crystals of $TbMn_{0.5}Fe_{0.5}O_3$ [34]. The onset of antiferromagnetic order begins at 286 K and a weak ferromagnetism begins to develop at 28 K along with a specific heat anomaly that can give a zero field cooled negative magnetization at this same temperature in 0.1 T that is not present in the field cooled data. The negative magnetization in $TbMn_{0.5}Fe_{0.5}O_3$ is considered to arise from domain wall pinning and there is a field dependence to the reversals. The element specific magnetization in that compound is yet to be determined. Electron doped manganites also showed negative magnetization, assigned to clusters, as in $CaMn_{1-x}Sb_xO_3$ [35]. Another recent report on air-fired neodymium orthomanganite [36] has presented a model-free description that attempts to contradict the domain/cluster model of off-stoichiometric $NdMnO_3$, although the data therein may be explained by considerations of stoichiometry as is discussed in Appendix B and by invoking a cluster model similar to $NdMnO_{3.11}$.

While the experimental data provide details of the neodymium magnetism and cannot be explained as competing sublattices but could be due to domain effects, the least clear aspect of this picture concerns the interaction between the iron-rich inclusions and the manganese-rich bulk. The cartoon asserts that magnetostatic domain formation is modified by the weak ferromagnetism in the iron-rich clusters, following the domain exchange bias arguments for why $NdMnO_{3.11}$ would show negative magnetization [22] but stoichiometric $NdMnO_3$ does not show negative magnetization [5]. However, these data are also consistent with some other domain wall pinning interaction besides inter-cluster superexchange that would also result from the inclusion of the foreign ions. Further study of this interaction could include measurements of large crystalline samples, $NdMn_{1-x}Zn_xO_3$ doping series to test if a magnetic interaction with the clusters is required for negative magnetization, or even smaller momentum transfers of a scattering experiment to better understand the spatial correlations of the clusters.

3. Conclusions

In summary, we have presented data that identify different elemental and spatial contributions to the magnetic response of **NMFO.2**. The previously ambiguous phase transition observed in **NMFO.2** at T = 15 K coincides with a ferromagnetically ordered neodymium moment in zero applied magnetic field as seen in these neutron backscattering data. The neodymium exchange field has been quantified with inelastic neutron scattering and has a temperature dependence that is correlated to the induced moment. The XMCD data show that the neodymium net magnetic moment evolves to be antiparallel to an applied field of 0.1 T on cooling into the magnetically ordered state. XMCD also shows that the neodymium net magnetic moments and manganese net magnetic moments in **NMFO.2** are parallel from H = 0.1 T to H = 2 T at T = 2 K, which rules out a competing sublattice model. Diffuse and small angle neutron scattering is assigned to short-range magnetic order that increases as the sample is cooled and is present in both **LMFO.2** and **NMFO.2**. The relative manganese and neodymium magnetic moment orientations along with the observation of magnetic clusters supports a domain picture for the reported negative magnetization in **NMFO.2**.

Neodymium, manganese, and iron ions all play leading roles in the magnetism of **NMFO.2.** The proposed model as iron-rich clusters that become frozen in above T_N and influence the domains of the manganese-rich bulk. In **LMFO.2** there is no magnetic compensation, while for **NMFO.2** the pinned domains from the onset of magnetic order are then trapped into a metastable configuration with the net moment against the applied field as the neodymium to manganese interaction causes a dramatic increase in the ferromagnetic moment. The negative magnetization can then be overcome with a sufficiently large external magnetic field. This description is supported by the experimental evidence presented in this manuscript and suggests a recipe to observe such an effect. Clusters must be present to pin the magnetic domains and the bulk of the material must experience an increase in ferromagnetism while cooling. Aside from negative magnetization, this type of embedded cluster system will also have the potential for increased magnetic hardness compared to the bulk phase due to the need to also reverse the domain pinning energy.

Declaration of Competing Interest

The authors declare that they have no known competing financial interests or personal relationships that could have appeared to influence the work reported in this paper.

Acknowledgements

The work at Oak Ridge National Laboratories' High Flux Isotope Reactor was supported by the United States Department of Energy (US-DOE), Office of Science – Basic Energy Science (BES), Scientific User Facilities Division. Access to HFBS was provided by the Center for High Resolution Neutron Scattering, a partnership between the National Institute of Standards and Technology and the National Science Foundation under Agreement No. DMR-1508249. Work at Argonne is supported by the U.S. Department of Energy, Office of Science, Office of Basic Energy Sciences, under Contract No. DE-AC-02-06CH11357. C.A.E. Jr. was supported by FAPESP (SP-Brazil) under Contract No. 2016/24137-3. Sample preparation at Argonne National Laboratory was supported by the U.S. Department of Energy, Office of Science, Basic Energy Sciences, Materials Science and Engineering Division. Work at IEP SAS is supported by the project VEGA 2/0137/19.

Appendix A:. Technical details

The **NMFO.2** ($NdMn_{0.8}Fe_{0.2}O_{3.065}$) sample is the same as in previous studies of $NdMn_{1-x}Fe_xO_{3+\delta}$ [8]. A detailed analysis of the relevant stoichiometry is given in Appendix B.

An analogue to **NMFO.2** without Nd magnetism was needed as a reference 'background' sample for inelastic neutron scattering measurements in order to isolate contributions from Nd. A La containing compound, $LaMn_{0.8}Fe_{0.2}O_{3+\delta}$ (**LMFO.2**), from the $LaMn_{1-x}Fe_xO_{3+\delta}$ (LMFO) series was targeted for this purpose. The polycrystalline compound was synthesized by solid state reaction using La_2O_3, MnO_2, and Fe_2O_3 as starting materials.

The mixture was reacted at 1300 °C for 10 h, reground, and fired again at 1400 °C for 12 h. Both firings occurred under flowing argon gas to minimize δ. On the basis of powder X-ray diffraction, the resulting material showed some phase separation between a perovskite phase of LMFO (likely with Fe content slightly higher than 0.2) and a coexisting perovskite phase with stoichiometry corresponding to approximately LMO. Some other dilute oxide impurities were observed at less than a percent by volume and would not be expected to influence the inelastic neutron scattering. The observation of a single magnetic ordering temperature in the NPD of **LMFO.2** presented below suggests a level of magnetic homogeneity high enough to serve as a suitable analogue to **NMFO.2**, at least for the purpose here of providing an approximation to the phonon neutron scattering contribution.

For neutron scattering, 10 g of powder samples were mounted in aluminum cans sealed in a helium atmosphere. For X-ray absorption measurements, five layers of finely ground powder mounted on tape were stacked to yield the desired sample thickness of ≈8 μm. This sample yielded an absorption edge jump of 1 across the Nd L_3 edge, 0.5 across the Nd L_2 edge, and 0.3 across the Mn K edge.

Neutron backscattering experiments were performed at the High Flux Backscattering Spectrometer (HFBS) at the National Institute of Standards and Technology Center for Neutron Research (NCNR) [37]. A Si(1 1 1) monochromator with a wavelength of 6.271 Å was used. The dynamic range of ± 5.7 μeV where the driving frequency is 8 Hz resulted in a full width half maximum (FHWM) resolution of 0.7 μeV as measured by the central (elastic) peak at base temperature. Peak positions were cross-checked with a dynamic range of ± 11 μeV, where the driving frequency employed was 15 Hz. The isotopes of Nd have the natural abundances of 12.18% for ^{143}Nd and 8.29% for ^{145}Nd, with incoherent cross sections of 55 ± 7 barns and 5 ± 5 barns, respectively [38]. Due to the larger abundance and cross section, nuclear spin scattering will be dominated by the ^{143}Nd species. Both ^{143}Nd and ^{145}Nd have nuclear moments of I = 7/2, which may couple to the electronic magnetic moments by way of the hyperfine coupling [12].

The X-ray absorption and XMCD measurements were carried out in transmission geometry. A liquid nitrogen cooled Si(1 1 1) double crystal monochromator was used to scan X-ray energy across the Nd L and Mn K edges. A pair of toroidal/flat Pd mirrors was used to reject higher energy harmonic content in the monochromatic X-ray beam as well as to focus the X-ray beam to a size of about 250 × 250 μm^2. Sample was mounted on the variable temperature insert of a cryomagnet and cooled in helium vapor. XMCD was measured in helicity switching mode, whereby the incident X-ray helicity was modulated at 13.1 Hz using a 180 μm-thick diamond C(1 1 1) phase retarder, the related modulation in X-ray absorption coefficient detected with a lock-in amplifier. A cryomagnet was used to apply a magnetic field aligned with the X-ray propagation direction. For data presentation, edge jumps were normalized to be 1 for each individual ion and this normalization is also applied to the respective XMCD signals. The Nd L_2 edge was chosen over the Nd L_3 edge due to the larger XMCD signal expected [39].

The Wide Angle Neutron Diffractometer (WAND) at the Oak Ridge National Laboratory (ORNL) High Flux Isotope Reactor (HFIR) was used to collect the NPD. The Ge (1 1 3) monochromator gave λ = 1.46 Å.

The Triple-Axis (TAX) spectrometer at the ORNL HFIR was used to probe the PINS of **NMFO.2** sample, along with that of the **LMFO.2** sample. Soller collimations of 48′-40′-40′-120′ were used between the reactor-mono-sample-analyzer-detector positions, respectively. A pyrolytic graphite filter was used behind the sample with a fixed final energy of E_f = 14.7 meV. The inelastic data are taken by sweeping the incident energy and dwelling at each energy while counting neutrons at the monitor until reaching a value associated with a fixed amount of time for a given reactor power. Counting at the monitor accounts for variations in flux, and the additional corrections of the $1/k_i$ monitor efficiency and higher order wavelength contamination from the monochromator are applied. The wavelength contamination correction was measured by using a mini-chopper in 2015, and a phenomenological fit of tanh(0.0495 × E_i)is used.

The SpinW libraries were used for the spin wave calculations [40]. The program SPECTRE was used for crystal field calculations [41]. Neutron specific constants were taken from the data booklet [42].

Appendix B:. Stoichiometry

Titration experiments show an oxygen excess that may be reported as $NdMn_{0.8}Fe_{0.2}O_{3.065\ \pm\ 0.006}$. Iron is assumed to be trivalent as Mössbauer spectroscopy on Fe doping into a similar manganite did not detect iron valence change [43]. Previously, stoichiometries of $LaMnO_{3+\delta}$ have been modeled as lanthanide and transition metal site vacancies [44], which would give

$$Nd^{3+}_{0.98}\#_{0.02}Mn^{4+}_{0.13}Mn^{3+}_{0.66}Fe^{3+}_{0.20}\#_{0.02}O^{2-}_{3}. \quad (1)$$

Alternatively, there was a study of the stoichiometry of air annealed NMO directly [45], which had a formula of

$$Nd^{3+}_{0.97}\#_{0.03}Mn^{4+}_{0.24}Mn^{3+}_{0.71}\#_{0.05}O^{2-}_{3}, \quad (2)$$

which further departs from the idealized formulation, but retains an Mn^{3+} majority on the transition metal site. For NMO, the unit cell volume, V_{NMO}, is another handle on the stoichiometry. An Ar-annealed NMO reported V_{NMO} = 0.2415 nm^3 ($V_{NMO}^{1/3}$ = 0.623 nm) [19]. On the other end of the spectrum, V_{NMO} = 0.2341 nm^3 ($V_{NMO}^{1/3}$ = 0.616 nm) was reported for $Nd_{0.97}Mn_{0.95}O_3$ (Eq. (3)) [45], which is similar to the unit cell volume reported for neutron powder diffraction on an NMO sample that showed a strong ferromagnetic component of the Mn site along the long axis [46]. The same preparation environment used for $NdMn_{0.8}Fe_{0.2}O_3$, but for the undoped NMO yielded V_{NMO} = 0.2383 nm^3 ($V_{NMO}^{1/3}$ = 0.620 nm) [5], for which a linear dependence of $V_{NMO}^{1/3}$ on Nd and Mn concentration would yield $Nd_{0.99}Mn_{0.98}O_3$ as

$$Nd^{3+}_{0.99}\#_{0.01}Mn^{4+}_{0.09}Mn^{3+}_{0.89}\#_{0.02}O^{2-}_{3}. \quad (3)$$

The precise crystallographic locations and macroscopic locations of the ions remains with some level of uncertainty, but it is likely that a small amount of Mn^{4+} may exist in the sample measured. The phase diagram of $\Xi = Mn^{4+}/(Mn^{3+} + Mn^{4+})$ concentration in perovskite-type manganites has shown distinct regions as a function of doping on the A-site [47]. In a pure manganite, the amount of Mn^{4+} in **NMFO.2** (Ξ = 0.13) would be near the boundary at Ξ = 0.1 between the Mn^{3+} dominant A-type antiferromagnetism ($\Xi < 0.1$) and a two phase sample that contains ferromagnetic clusters within a sea of A-type antiferromagnetism ($\Xi > 0.1$). However, there has not been a study of the phase boundary position dependence upon iron doping.

Appendix C. Supplementary data

Supplementary data to this article can be found online at https://doi.org/10.1016/j.jmmm.2019.165968.

References

[1] M.B. Salamon, M. Jaime, Rev. Mod. Phys. 73 (2001) 583.
[2] A.P. Ramirez, J. Phys. Condens. Matter 9 (1997) 8171.
[3] K. Liu, X.W. Wu, K.H. Ahn, T. Sulchek, C.L. Chien, J.Q. Xiao, Phys. Rev. B 54 (1996) 3007.
[4] I.O. Troyanchuk, M.V. Bushinsky, H. Szymczak, M. Baran, K. Bärner, J. Magn. Magn. Mater. 312 (2007) 470.
[5] M. Mihalik, M. Mihalik, M. Fitta, M. Bałanda, M. Vavra, S. Gabáni, M. Zentková, J. Briančin, J. Magn. Magn. Mater. 345 (2013) 125.
[6] J. Lazurova, M. Mihalik, M. Mihalik Jr, M. Vavra, M. Zentkova, J. Briancin, M. Perovic, V. Kusigerski, O. Schneeweiss, P. Roupcova, K.V. Kamenev, M. Misek, Z. Jaglicic, J. Phys. Conf. Ser. 592 (2015) 012117.
[7] A. Singh, A. Jain, A. Ray, B. Padmanabhan, R. Yadav, V. Nassif, S. Husain, S.M. Yusuf, T. Maitra, V.K. Malik, Phys. Rev. B 96 (2017) 144420.
[8] M. Mihalik, M. Mihalik, A. Hoser, D.M. Pajerowski, D. Kriegner, D. Legut, K.M. Lebecki, M. Vavra, M. Fitta, M.W. Meisel, Phys. Rev. B 96 (2017) 134430.
[9] W. Tong, B. Zhang, S. Tan, Y. Zhang, Phys. Rev. B 70 (2004) 014422.
[10] A.K. Kundu, R. Ranjith, B. Kundys, N. Nguyen, V. Caignaert, V. Pralong, W. Prellier, B. Raveau, Appl. Phys. Lett. 93 (2008) 052906.
[11] A. Kumar, S.M. Yusuf, Phys. Rep. 556 (2015) 1.
[12] R.L. Carlin, Magnetochemistry, Springer-Verlag, Berlin; New York, 1986.
[13] S. Geller, E.A. Wood, Acta Crystallogr. 9 (1956) 563.
[14] N. Koshizuka, K. Hayashi, J. Phys. Soc. Japan 57 (1988) 4418.
[15] K.P. Belov, A.K. Zvezdin, A.M. Kadomtseva, R.Z. Levitin, Sov. Phys. Usp. 19 (1976) 574.
[16] J. Bartolomé, E. Palacios, M.D. Kuz'min, F. Bartolomé, I. Sosnowska, R. Przeniosło, R. Sonntag, M.M. Lukina, Phys. Rev. B 55 (1997) 11432.
[17] R. Przeniosło, I. Sosnowska, B. Frick, J. Magn. Magn. Mater. 305 (2006) 186.
[18] S.J. Yuan, W. Ren, F. Hong, Y.B. Wang, J.C. Zhang, L. Bellaiche, S.X. Cao, G. Cao, Phys. Rev. B – Condens. Matter Mater. Phys. 87 (2013) 1.
[19] T. Chatterji, B. Ouladdiaf, D. Bhattacharya, J. Phys. Condens. Matter 21 (2009) 306001.
[20] W. Sławiński, R. Przeniosło, I. Sosnowska, E. Suard, J. Phys. Condens. Matter 17 (2005) 4605.
[21] T. Chatterji, G.J. Schneider, L. van Eijck, B. Frick, D. Bhattacharya, J. Phys. Condens. Matter 21 (2009) 126003.
[22] F. Bartolomé, J. Herrero-Albillos, L.M. García, J. Bartolomé, N. Jaouen, A. Rogalev, J. Appl. Phys. 97 (2005).
[23] I.O. Troyanchuk, V.A. Khomchenko, G.M. Chobot, A.I. Kurbakov, A.N. Vasil'ev, V.V. Eremenko, V.A. Sirenko, M.Y. Shvedun, H. Szymczak, R. Szymczak, J. Physics-Condensed Matter 15 (2003) 8865.
[24] G. Shirane, S. Shapiro, J. Tranquada, Neutron Scattering with a Triple-Axis Spectrometer, Cambridge University Press, Cambridge, 2004.
[25] A. Podlesnyak, S. Rosenkranz, F. Fauth, W. Marti, A. Furrer, A. Mirmelstein, H.J. Scheel, J. Phys. Condens. Matter 5 (1993) 8973.
[26] R. Przeniosło, I. Sosnowska, M. Loewenhaupt, A. Taylor, J. Magn. Magn. Mater. 140144 (1995) 2151.
[27] Supplementary materials are available online at ….
[28] S. Jandl, V. Nekvasil, M. Diviš, A.A. Mukhin, J. Hölsä, M.L. Sadowski, Phys. Rev. B 71 (2005) 024417.
[29] E. Jones, T. Oliphant, P. Peterson, SciPy Open Source Sci. Tools Python (2001).
[30] F. Bartolomé, J. Bartolomé, J. Campo, Phys. B Condens. Matter 312–313 (2002) 769.
[31] S. Mertens, J. Stat. Phys. 58 (1990) 1095.
[32] D.M. Pajerowski, Phys. Rev. B 98 (2018) 134431.
[33] Y. Deng, H.W.J. Blöte, Phys. Rev. E 72 (2005) 016126.
[34] H. Nhalil, H.S. Nair, S.R.A.M. Strydom, S. Elizabeth, J. Appl. Phys. 117 (2015) 173904.
[35] Y. Murano, M. Matsukawa, S. Ohuchi, S. Kobayashi, S. Nimori, R. Suryanarayanan, K. Koyama, N. Kobayashi, Phys. Rev. B – Condens. Matter Mater. Phys. 83 (2011) 1.
[36] A. Kumar, S.M. Yusuf, C. Ritter, Phys. Rev. B 96 (2017) 1.
[37] A. Meyer, R.M. Dimeo, P.M. Gehring, D.A. Neumann, Rev. Sci. Instrum. 74 (2003) 2759.
[38] V.F. Sears, Neutron News 3 (1992) 26.
[39] M. van Veenendaal, J.B. Goedkoop, B.T. Thole, Phys. Rev. Lett. 78 (1997) 1162.
[40] S. Toth, B. Lake, J. Phys. Condens. Matter 27 (2015).
[41] A. Boothroyd, 1 (2015).
[42] H. Börner, J. Brown, C.J. Carlile, R. Cubitt, R. Currat, A.J. Dianoux, B. Farago, A.W. Hewat, J. Kulda, E. Lelièvre-Berna, G.J. McIntyre, S.A. Mason, R.P. May, A. Oed, J.R. Stewart, F. Tasset, J. Tribolet, I. Anderson, D.W. Dubbers, Neutron Data Booklet, Old City Publishing, Philadelphia, PA, 2003.
[43] L.K. Leung, A.H. Morrish, B.J. Evans, Phys. Rev. B 13 (1976) 4069.
[44] J.A.M. van Roosmalen, E.H.P. Cordfunke, J. Solid State Chem. 110 (1994) 109.
[45] V.A. Cherepanov, L.Y. Barkhatova, A.N. Petrov, V.I. Voronin, J. Solid State Chem. 118 (1995) 53.
[46] A. Muñoz, J.A. Alonso, M.J. Martínez-Lope, J.L. García-Muñoz, M.T. Fernández-Díaz, J. Phys. Condens. Matter 12 (2003) 1361.
[47] J.B. Goodenough, Phys. Rev. 100 (1955) 564.